



This is a repository copy of *Visualization and chemical characterization of the cathode electrolyte interphase using He-ion microscopy and in situ time-of-flight secondary ion mass spectrometry*.

White Rose Research Online URL for this paper:  
<http://eprints.whiterose.ac.uk/167744/>

Version: Published Version

---

**Article:**

Wheatcroft, L., Klingner, N., Heller, R. et al. (4 more authors) (2020) Visualization and chemical characterization of the cathode electrolyte interphase using He-ion microscopy and in situ time-of-flight secondary ion mass spectrometry. *ACS Applied Energy Materials*, 3 (9). pp. 8822-8832. ISSN 2574-0962

<https://doi.org/10.1021/acsaem.0c01333>

---

**Reuse**

This article is distributed under the terms of the Creative Commons Attribution (CC BY) licence. This licence allows you to distribute, remix, tweak, and build upon the work, even commercially, as long as you credit the authors for the original work. More information and the full terms of the licence here:  
<https://creativecommons.org/licenses/>

**Takedown**

If you consider content in White Rose Research Online to be in breach of UK law, please notify us by emailing [eprints@whiterose.ac.uk](mailto:eprints@whiterose.ac.uk) including the URL of the record and the reason for the withdrawal request.



[eprints@whiterose.ac.uk](mailto:eprints@whiterose.ac.uk)  
<https://eprints.whiterose.ac.uk/>

# Visualization and Chemical Characterization of the Cathode Electrolyte Interphase Using He-Ion Microscopy and *In Situ* Time-of-Flight Secondary Ion Mass Spectrometry

Laura Wheatcroft,\* Nico Klingner, René Heller, Gregor Hlawacek, Doğan Özkaya, James Cookson, and Beverley J. Inkson

Cite This: *ACS Appl. Energy Mater.* 2020, 3, 8822–8832

Read Online

ACCESS |

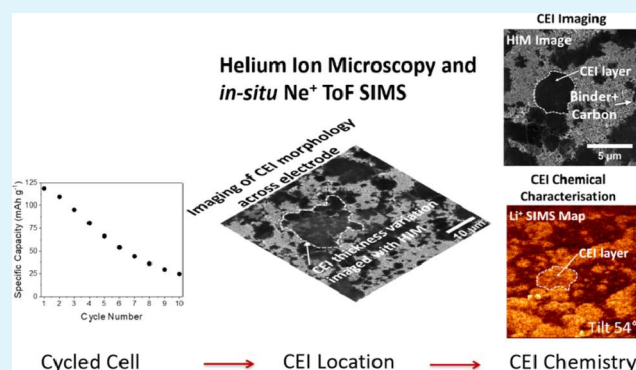
Metrics & More

Article Recommendations

Supporting Information

**ABSTRACT:** Unstable cathode electrolyte interphase (CEI) formation increases degradation in high voltage Li-ion battery materials. Few techniques couple characterization of nano-scale CEI layers on the macroscale with *in situ* chemical characterization, and thus, information on how the underlying microstructure affects CEI formation is lost. Here, the process of CEI formation in a high voltage cathode material, LiCoPO<sub>4</sub>, has been investigated for the first time using helium ion microscopy (HIM) and *in situ* time-of-flight (ToF) secondary ion mass spectrometry (SIMS). The combination of HIM and Ne-ion ToF-SIMS has been used to correlate the cycle-dependent morphology of the CEI layer on LiCoPO<sub>4</sub> with a local cathode microstructure, including position, thickness, and chemistry. HIM imaging identified partial dissolution of the CEI layer on discharge resulting in in-homogenous CEI coverage on larger LiCoPO<sub>4</sub> agglomerates. Ne-ion ToF-SIMS characterization identified oxyfluorophosphates from HF attack by the electrolyte and a Li-rich surface region. Variable thickness of the CEI layer coupled with inactive Li on the surface of LiCoPO<sub>4</sub> electrodes contributes to severe degradation over the course of 10 cycles. The HIM–SIMS technique has potential to further investigate the effect of microstructures on CEI formation in cathode materials or solid electrolyte interphase formation in anodes, thus aiding future electrode development.

**KEYWORDS:** lithium ion batteries, SEI/CEI layer, helium ion microscopy, ToF-SIMS, surface degradation imaging and chemical characterization



## 1. INTRODUCTION

The electrification of transport is being implemented as a method to significantly reduce fossil fuel consumption. Li-ion batteries are a potential solution to power electric vehicles (EVs) because of their high theoretical specific energy (up to 300 W h kg<sup>-1</sup>),<sup>1</sup> but experimentally achieved energy density increases are required to extend the EV driving range.<sup>2</sup> One method of improving the specific energy is to raise the operating potential of the individual battery cells, requiring the development of new cathode materials and electrolyte systems which have a nominal operating potential (potential where redox occurs) and stability greater than 4.5 V versus Li/Li<sup>+</sup>.

LiCoPO<sub>4</sub> (LCP) is a high voltage Li-ion cathode material initially developed in 2000 by Amine et al.<sup>4</sup> LiCoPO<sub>4</sub> has a high theoretical capacity (167 mA h g<sup>-1</sup>) coupled with a high nominal operating potential (4.8 V vs Li/Li<sup>+</sup>).<sup>5</sup> Taking the high redox potential and capacity into account and despite the higher cost of Co compared to other transition metals typically used in Li-ion cathode materials, the cost per energy of the overall LCP cell is lower compared with other cathode

materials (LiCoO<sub>2</sub>).<sup>5</sup> Therefore, there is significant interest in the development and optimization of LiCoPO<sub>4</sub> cathodes for electric vehicle applications.

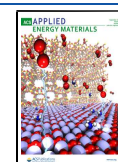
Despite the benefits LiCoPO<sub>4</sub> could offer, it has not been commercialized because of the poor rate performance and capacity fading when cycling.<sup>5</sup> The causes of poor cyclability have been attributed to structural issues such as anti-site defect formation blocking Li from migrating via the ion transport channels in the crystal structure<sup>6,7</sup> and electrolyte degradation due to high operating potentials.<sup>8</sup>

LiCoPO<sub>4</sub> cathodes are commonly used with LiPF<sub>6</sub>-based electrolytes in carbonate solutions, which can become unstable at higher voltages forming HF, F<sup>-</sup> anions and a number of

Received: June 8, 2020

Accepted: August 25, 2020

Published: August 25, 2020



carbonate species.<sup>8,9</sup> Upon de-lithiation, LiCoPO<sub>4</sub> forms a less stable CoPO<sub>4</sub> phase.<sup>5</sup> The P–O bonds in CoPO<sub>4</sub> can undergo a nucleophilic attack from F<sup>−</sup> anions, resulting in the formation of soluble LiPO<sub>2</sub>F<sub>2</sub>, leading to dissolution of the cathode material and the associated capacity fade.<sup>8,10</sup>

The reactions on cathode surfaces caused by electrolyte breakdown can also result in surface film formation called the cathode electrolyte interphase (CEI)<sup>11</sup> (or solid electrolyte interphase (SEI) on anodes). The formation of CEIs can be beneficial in terms of capacity fade as they can act as passivation layers against parasitic reactions from the electrolyte.<sup>11</sup> However, CEI formation can hinder performance, particularly if Li is consumed in its formation, and the CEI layer continues to thicken with further cycling.<sup>12</sup> CEI thickening has been observed in LiCoPO<sub>4</sub> by postmortem transmission electron microscopy analysis.<sup>13</sup> If the CEI layer becomes too thick, it can become detrimental to battery performance because of the need for lithium ions to diffuse through the layer.

Electrodes are a complex composite of active materials (such as LiCoPO<sub>4</sub>), conductive additives, and binders. There is a current debate about where the CEI layers form on the cathode, either solely on LiCoPO<sub>4</sub><sup>13</sup> or also involving the conductive additive.<sup>11</sup> In order to fully understand how the underlying cathode microstructure affects the CEI formation, ideal characterization techniques should correlate high-resolution surface imaging with chemical characterization techniques.

Studying CEI layers is challenging because they are air sensitive, they contain Li, and they are thin films on top of complex surfaces. Most LiCoPO<sub>4</sub> CEI layer studies have focused on spatially averaged chemical analysis using techniques such as X-ray photoelectron spectroscopy (XPS) and Raman spectroscopy.<sup>9,11</sup> Techniques such as scanning electron microscopy (SEM) and transmission electron microscopy (TEM)<sup>13</sup> are typically employed for postmortem chemical analysis microstructural imaging when the layer is thick enough to provide significant contrast. However, for cathode materials, often the CEI layer is very thin, requiring microscopies with higher surface resolution than SEM for detection.<sup>14</sup>

Helium ion microscopy (HIM) is a recently introduced technique where He<sup>+</sup> or Ne<sup>+</sup> gas ions are used for focused ion beam (FIB) microscopy. He<sup>+</sup> ion-induced secondary electron (He-iSE) imaging uses surface sensitive SE1 electrons for image formation. Ion interaction with the surface results in a smaller spot size compared to electron induced secondary electron imaging (eSE).<sup>15</sup> The combination of SE1 imaging and a small spot size results in higher surface sensitivities and spatial resolutions than SEM, and thus, HIM has been used extensively in Si microchip research.<sup>16–18</sup> He<sup>+</sup> or Ne<sup>+</sup> ion-induced secondary electron (He/Ne-iSE) images are used interchangeably, depending on the resolution and/or chemical analysis requirements. For chemical analysis, time-of-flight secondary ion mass spectrometry (ToF-SIMS) for helium ion microscopy (HIM), using an incident He<sup>+</sup> or Ne<sup>+</sup> beam, has been developed by Klingner and co-workers.<sup>19,20</sup> The combination of high-resolution surface imaging provided by HIM and ToF SIMS within the helium ion microscope capable of detecting Li<sup>+</sup> makes HIM–SIMS a potentially powerful technique to study CEI layers on lithium ion battery cathodes.

In this paper, we evaluate the nanoscale growth mechanisms of the CEI on high voltage LiCoPO<sub>4</sub> cathodes as a function of

electrode cycling history. In particular, we correlate the morphology of CEI growth on LiCoPO<sub>4</sub> with the chemistry of the electrode surface, that is, the CEI composition and its location on the electrode with respect to the active material or conductive additive, using high spatial resolution helium ion imaging and Ne-ion ToF-SIMS for HIM.<sup>19,20</sup>

## 2. EXPERIMENTAL SECTION

**2.1. Electrode Manufacture.** LiCoPO<sub>4</sub> is often coated with a thin carbon layer to increase the electrical conductivity of LiCoPO<sub>4</sub> electrodes.<sup>5</sup> Here, carbon-coated LiCoPO<sub>4</sub> (C-LiCoPO<sub>4</sub>) was used for the experiments, with a thickness of 2–8 nm (as measured by TEM).

Composite electrodes with a composition of 90 wt % C-LiCoPO<sub>4</sub> (Johnson Matthey), 5 wt % polyvinylidene fluoride (PVDF) binder (MTI), and 5 wt % Super C65 conductive additive (C.Nergy TIMCAL) were manufactured using a tape casting method. A slurry of C-LiCoPO<sub>4</sub>, PVDF, and C65 with *N*-methyl-2-pyrrolidone (NMP) (Sigma-Aldrich) as a solvent was mixed with an orbital mixer (Thinky). The PVDF binder was predissolved in NMP to make a 10 wt % solution. The components were gradually added with an additional solvent to ensure an even distribution of the binder, conductive additive, and active material. The total mixing time was 16 min. The resulting slurry was spread to 200 μm thickness using a doctor blade on carbon coated Al (MTI). The electrode sheets were calendared using a hot roller (MTI) sandwiched between two stainless steel sheets and Al foil (Al foil touching the electrode surface) to obtain electrode densities between 1.7 and 1.9 g cm<sup>−3</sup>. The electrodes were punched into 12 mm diameter discs ready for assembly into cells.

The electrodes were assembled into half cells using the Li metal (Sigma Aldrich) as a counter electrode with a Whatman GF/F separator and Celgard 2325 separator with 160 μL of LiPF<sub>6</sub> in 50/50 volume ratio of ethylene carbonate and dimethyl carbonate (DMC) (Sigma-Aldrich) electrolytes. The cells were sealed in CR2016 coin-cells (Cambridge Energy Solutions) in an argon filled glove box. The atmosphere was controlled to contain <0.1 ppm O<sub>2</sub> and H<sub>2</sub>O.

**2.2. Electrochemical Testing.** Galvanostatic cycling up to 10 cycles, at 0.1 C between 2.5 and 5.1 V versus Li/Li<sup>+</sup>, was performed using a Maccor galvanostat. The C-rate was calculated from the theoretical capacity of LiCoPO<sub>4</sub> (167 mA h g<sup>−1</sup>).<sup>5</sup> After each galvanostatic charge step, the cell was charged potentiostatically at 5.1 V versus Li/Li<sup>+</sup> to ensure complete charging. After cycling, the coin cells were disassembled in an argon filled glove box, and electrodes were rinsed with DMC (Sigma-Aldrich) to remove the liquid electrolyte. The electrodes were mounted onto SEM stubs in the glove box and sealed into air-tight bags for transport to the helium ion microscope. On transferring to the helium ion microscope, the electrodes were briefly exposed to air (<1 min) as there was no access to a vacuum transfer system.

**2.3. HIM-TOF-SIMS Analysis of CEI Layers.** HIM analysis of cycled electrodes was performed in a Zeiss Orion NanoFab helium ion microscope. Imaging was performed with a He<sup>+</sup> beam at 25 keV as the incident focused ion beam and the ion-induced secondary electrons (iSEs) were detected with an Everhart–Thornley detector (ETD).

*In situ* ToF-SIMS measurements were performed with a ToF-SIMS detector in the helium ion microscope designed and built by Klingner et al.<sup>19,20</sup> Secondary ions were sputtered using 25 keV Ne<sup>+</sup> ions as incident ions. Site-specific mass spectra, lateral ion distribution maps, and depth profiles of both positive and negative secondary ions were collected from different areas of the cycled electrodes.

ToF-SIMS measurements were enabled by pulsing the primary Ne<sup>+</sup> ion beam while biasing the sample to either plus or minus 500 V. The specimen stage was tilted by 54° to position the sample surface perpendicular to the secondary ion extraction optics. Sputtered ions with the same polarity as the bias voltage are accelerated into the spectrometer and focused by an Einzel lens. The extracted secondary ions with different mass and therefore velocity separate in a flight tube

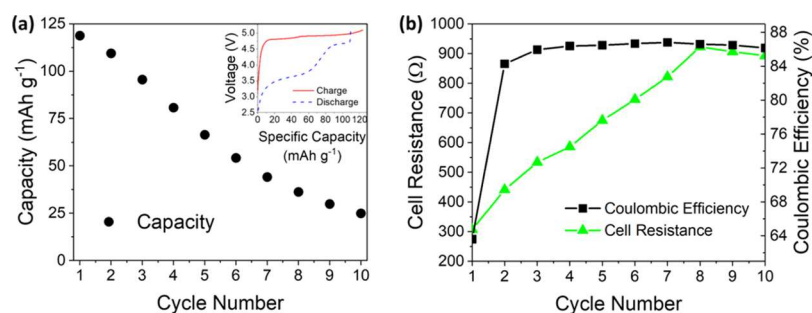


**Figure 1.** Representative electrochemical behavior of C-LiCoPO<sub>4</sub> electrodes at 0.1 C. (a) Variation of specific capacity with the cycle number, (a-inset) galvanostatic charge and discharge curve on the second cycle, (b) Coulombic efficiency and overall cell resistance calculated from the voltage drop on the galvanostatic charge and discharge curves.

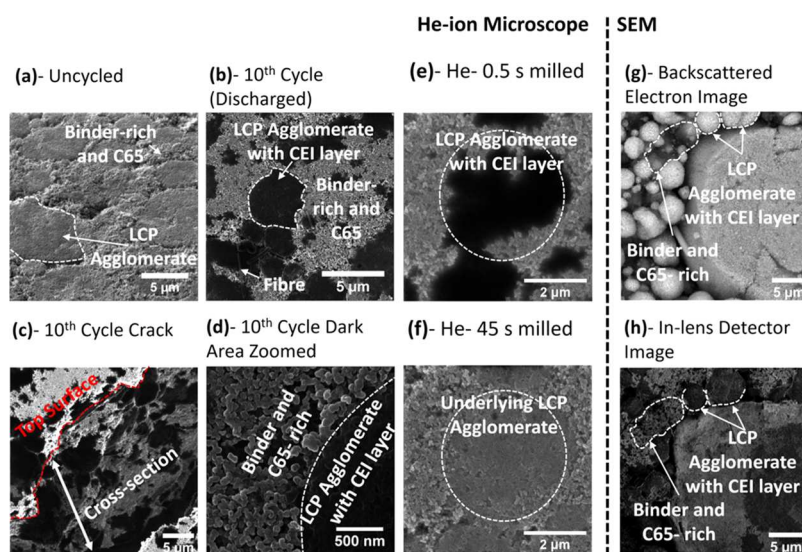


**Figure 2.** HIM He-iSE images of (a) uncycled electrode surface tilted to 54°, (b) electrode surface of the 10th cycle discharged electrode, (c) crack in the surface of the 10th cycle discharged electrode, showing the cross section through the electrode, and (d) a higher magnification image of the top surface of the 10th cycle discharged electrode. (e,f) He-iSE images of the surface after 0.5 s He<sup>+</sup> milling (e) and 45 s He<sup>+</sup> milling (f). SEM images of the top surface of the 10th cycle discharged electrode using (g) a backscattered electron image and (h) in-lens secondary electron image. Fiber in (b) originates from the fiber-glass separator.

and are detected at the end of the spectrometer with a microchannel plate.<sup>19</sup> Spectra were collected by applying Ne<sup>+</sup> ion pulses per pixel with a pulse length of 50 to 150 ns. For SIMS depth profiling the measured area was overscanned by 100%, with the analyzed area at the center and with an unblanked beam for ~100 μs per pixel.

In order to identify the mass to charge ratios of the SIMS peaks, the spectra were calibrated using software developed by Klingner *et al.*<sup>19</sup> Calibration was performed so that each peak correlated to within 0.2 u of an integer (as mass/charge ratios must be integers, 0.5, 0.33, or 0.66 depending on the ion charge). As this is the first Ne<sup>+</sup> ion SIMS analysis of the C-LiCoPO<sub>4</sub> CEI layer chemistry, the SIMS spectra were compared with previous Cs<sup>+</sup> ion SIMS analysis of high-voltage Li-ion battery electrodes using the same electrolyte LP-30 to identify the *m/z* ratio ion fragments.<sup>12</sup> The results were also compared with previous XPS studies on C-LiCoPO<sub>4</sub> to help identify the composition of the CEI layer.<sup>11</sup>

**2.4. Electron Microscopy Analysis of CEI Layers.** SEM images of the cycled electrodes were taken with a FEI Helios NanoLab G3 UC using an in-lens detector (ILD) and an ETD for electron induced secondary electron imaging (eSE) and a backscattered secondary electron (BSE) detector. The eSE images were collected at different beam currents and voltages to evaluate optimum CEI imaging conditions.

For higher spatial resolution imaging, scanning transmission electron microscopy (STEM), high angle annular dark field (HAADF), and bright field (BF) images were taken with a JEOL

JEM F200 transmission electron microscope at 200 keV using Gatan HAADF and JEOL BF detectors. Samples were prepared by scraping and grinding dried electrodes onto a TEM grid in an Ar-filled glove box and transferring into the microscope. The samples were briefly exposed to air on transfer (<1 min).

### 3. RESULTS AND DISCUSSION

**3.1. Electrochemical Testing.** Typical electrochemical characteristics of a C-LiCoPO<sub>4</sub> half-cell are shown in Figure 1. All cells tested and analyzed *ex situ* show similar characteristics. The initial specific capacity was on average (118 ± 4) mA h g<sup>-1</sup>. By the 10th cycle, the half-cell in Figure 1a had lost 79% of its initial capacity, indicating severe degradation similar to previous studies on C-LiCoPO<sub>4</sub> in LiPF<sub>6</sub> EC/DMC electrolytes.<sup>8,21</sup> An atypical charging plateau occurred at 3.5 V versus Li/Li<sup>+</sup> on discharge, which has been previously reported.<sup>22</sup> The electrodes here had been calendared in order to improve their electrical conductivity, and the atypical plateau became significant after calendaring (see Supporting Information). In this work, no impurities were detected by XRD, SIMS, or TEM imaging (see Supporting Information).

Cell resistance was measured from the voltage drop in the galvanostatic cycling curves. Overall cell resistance increased as

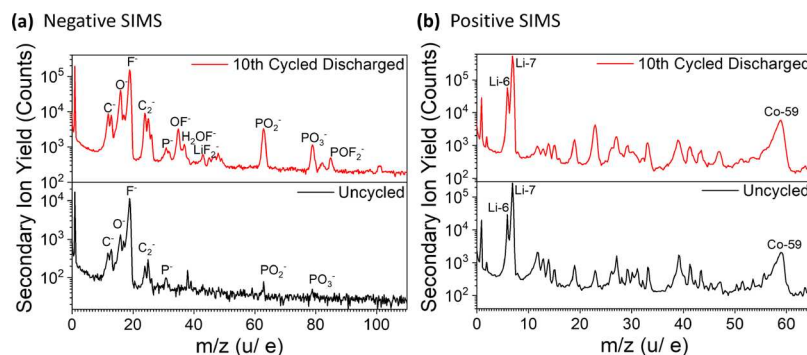


**Figure 3.** Ne-ion secondary ion mass spectra of the top surface of an uncycled electrode and the 10th cycled electrode in (a) negative and (b) positive modes.

the capacity dropped but stabilized at cycle 8 (Figure 1a,b). A low initial coulombic efficiency (64%) was observed on the first cycle indicating Li consumption. This behavior has been previously attributed to the formation of the CEI layer on the first cycle.<sup>11,23</sup> Coulombic efficiency stabilized to 86%, lower than that needed for a commercial cell and a further indicator of degradation processes which prevent Li insertion and de-insertion in the electrode occurring.

**3.2. Microstructural Characterization with HIM and SEM.** To determine the mechanisms of electrode degradation, electrode microstructures were characterized by HIM after different degrees of cycling. Uncycled electrodes (Figure 2a) exhibited two types of surface morphologies, smooth round regions with rougher regions in-between, corresponding to C-LiCoPO<sub>4</sub> agglomerates, and C65- and binder-rich regions.

Changes to the electrode surface microstructure occurred after cycling for 10 cycles (and in the discharged state) and were identified using HIM He<sup>+</sup>iSE imaging (Figure 2b–d). Distinct regions of dark contrast, due to low efficiency to extract ion-induced secondary electron because of positive sample charging, were observed on the surface of the cycled electrodes, (Figure 2b) which were not present on the surface of uncycled electrodes using comparable incident He<sup>+</sup>-ion beam conditions (Figure 2a). Higher magnification imaging (Figure 2d) and He<sup>+</sup> milling through the dark contrast region (Figure 2e,f) confirm the contrast difference results from the presence of a surface film.

Figure 2c is an image of a crack in the electrode, showing a cross-section through the electrode thickness. The large crack formed as a result of tearing the electrode after de-crimping. Patches of the dark contrast film extend through the cross-section of the electrode (Figure 2c), as well as the top surface, and are consistent with a CEI layer as the layer is present on regions where the electrolyte had contact with the electrode under high potentials.

The CEI layer is heterogeneous across the surface of the cycled electrode and is present mostly as circular patches ranging from 300 to 0.2 μm<sup>2</sup> (Figure 2b,c). Using SEM backscattered electron imaging Figure 2g, C-LiCoPO<sub>4</sub> agglomerates (bright contrast from high Z Co) can be clearly distinguished from the binder- and C65-rich regions (dark contrast from low average Z). The CEI film is visible using SEM with secondary electron (eSE) imaging using an ILD at low beam currents and voltages (Figure 2h). Comparison of an eSE ILD image (Figure 2h) with a backscattered electron image of the same region (Figure 2g) confirms that the CEI layer forms on C-LiCoPO<sub>4</sub> agglomerates, which explains the

predominant round shape of the dark contrast regions on the HIM images. CEI formation on C-LiCoPO<sub>4</sub> is similar to the results found with TEM imaging in the literature.<sup>11</sup>

Comparison between BSE and eSE electrode imaging (Figure 2g,h) also shows that the CEI does not uniformly cover the entire surface of the LCP agglomerates. The large ~20 μm C-LiCoPO<sub>4</sub> agglomerate in Figure 2h exhibits regions of both low and high eSE yield. The mottled eSE contrast in the predominant bright contrast outer edge of the large agglomerate in Figure 2h may indicate that the CEI layer is thinner in this region. CEI layers would be expected to form anywhere that is electrochemically active,<sup>24</sup> so this observation is surprising, suggesting that CEI layer formation is not homogenous in C-LiCoPO<sub>4</sub>. Given the instability of the delithiated phase of LiCoPO<sub>4</sub>, CoPO<sub>4</sub> found in these electrodes (see Supporting Information) with the electrolyte,<sup>8</sup> any direct exposure to the electrolyte from insufficient CEI coverage is likely to result in additional degradation.

He<sup>+</sup> iSE imaging provides higher resolution imaging of the electrode and CEI layer microstructure than SEM imaging (Figure 2). This is due to the very small He<sup>+</sup> ion spot size and highly localized iSE escape volume and because He<sup>+</sup> iSE images are formed mostly of SE1 electrons which are generated by direct interaction of the ion beam with the electrode surface.<sup>17</sup>

**3.3. Chemical Characterization with Secondary Ion Mass Spectrometry.** Ne-ion ToF-SIMS is used here as a new method to enable site-specific chemical characterization of the electrode surface. Ion fragments have been identified based on other high voltage cathode CEI Cs<sup>+</sup> ToF SIMS work by Manthiram *et al.*<sup>12</sup> Figure 3 shows the positive (a) and negative (b) Ne<sup>+</sup> ion SIMS spectra of an uncycled electrode and an electrode at the 10th cycle in the discharged state. The peaks identified on the SIMS spectra in Figure 3 were consistent across three regions of the same sample. SIMS was repeated on two, 10th cycle discharged electrodes, and the same significant peaks were found. The positive spectra do not vary significantly between the cycled and uncycled electrode, with significant peaks at 6 u/e (<sup>6</sup>Li<sup>+</sup>), 7 u/e (<sup>7</sup>Li<sup>+</sup>), and 59 u/e (<sup>59</sup>Co<sup>+</sup>). The negative spectra are distinctly different, containing peaks from the cycled electrode which were not present in the uncycled C-LiCoPO<sub>4</sub> electrode at 35 u/e (<sup>16</sup>O<sup>19</sup>F<sup>-</sup>), 37 u/e (<sup>1</sup>H<sub>2</sub><sup>16</sup>O<sup>19</sup>F<sup>-</sup>), 45 u/e (<sup>7</sup>Li<sup>19</sup>F<sub>2</sub><sup>-</sup>), and 85 u/e (<sup>31</sup>P<sup>16</sup>O<sup>19</sup>F<sub>2</sub><sup>-</sup>).

The unique advantage of using ToF-SIMS in HIM for CEI characterization is the direct high spatial resolution correlation of microstructure changes with associated changes in

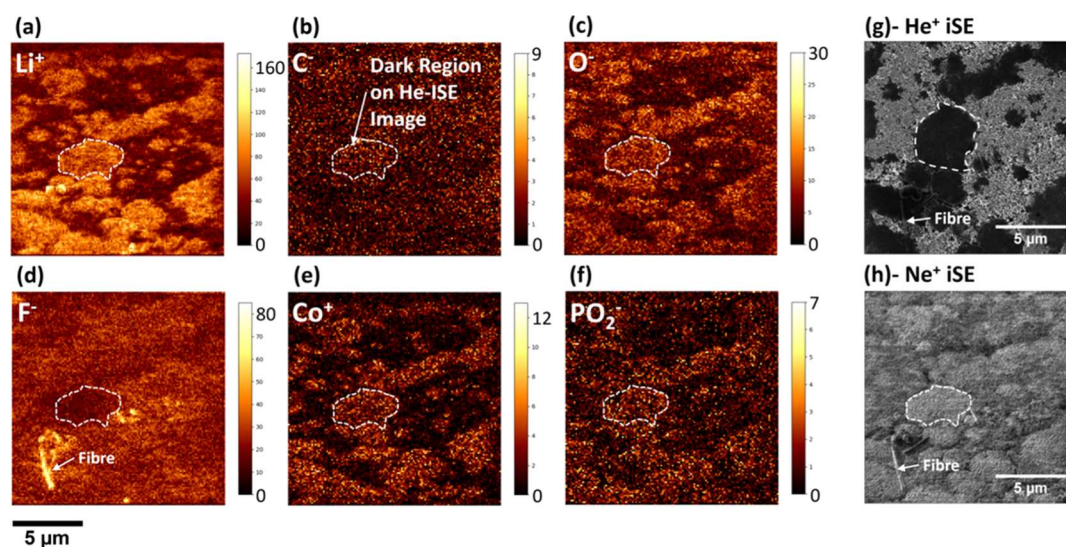


**Figure 4.** Ne-SIMS maps of the chemistry of the electrode top surface of the 10th cycle discharged electrode imaged at a tilt angle of  $54^\circ$ . The color gradient scales correspond to the secondary ion counts per pixel. The SIMS maps presented are (a) 7 u/e ( $\text{Li}^+$ ), (b) 12 u/e ( $\text{C}^-$ ), (c) 16 u/e ( $\text{O}^-$ ), (d) 19 u/e ( $\text{F}^-$ ), (e) 59 u/e ( $\text{Co}^+$ ), and (f) 63 u/e ( $\text{PO}_2^-$ ). The white dotted circle represents the same CEI layer region, also circled on the corresponding  $\text{He}^+$ -iSE (g) and  $\text{Ne}^+$ -iSE (h) image. The  $\text{He}^+$ -iSE image in (g) is at normal incidence.

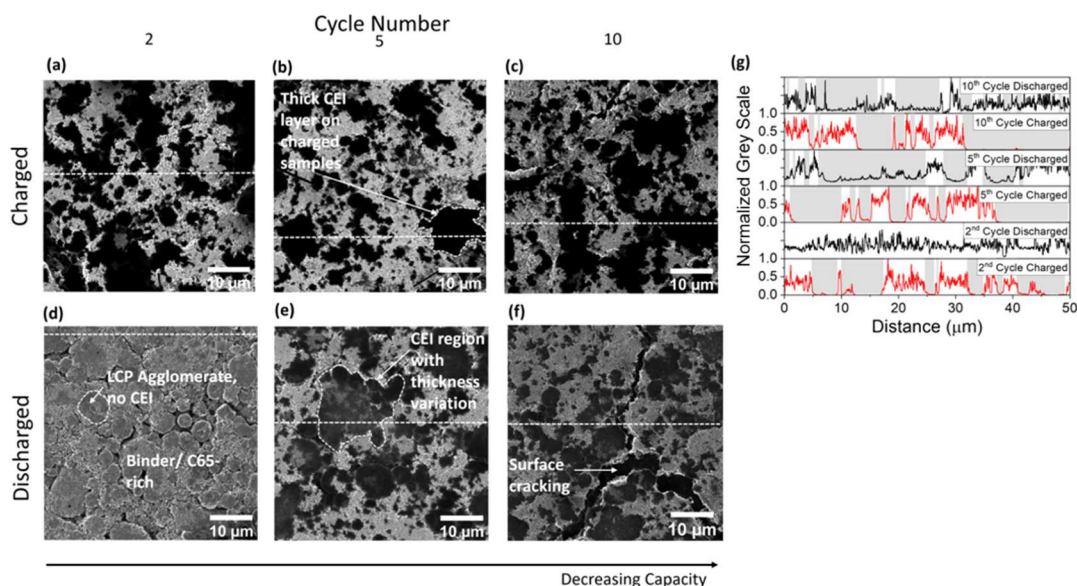


**Figure 5.** (a–f)  $\text{He}^+$  iSE images of the top surface of cycled electrodes showing the variation in the microstructure with the cycle number and state of charge. Dark contrast (low iSE yield) corresponds to the CEI layer and light contrast (high iSE yield) corresponds to binder-/C65-rich regions. “Charged” samples (a–c) were charged to 5.1 V vs  $\text{Li}/\text{Li}^+$  and de-primed on the cycle number shown. Similarly, “discharged” samples (d–f) were discharged to 2.5 V versus  $\text{Li}/\text{Li}^+$  on the cycle number shown. (g) Normalized grey scale contrast line profiles taken from the  $\text{He}^+$ -iSE images in (a–f), along the white dotted lines. The grey scale has been normalized to the maximum intensity for each image. The grey boxes indicate CEI layer regions detected on electrode surfaces.

chemistry, including Li distribution, using SIMS mapping (Figure 4). The SIMS presented here is  $\text{Ne}^+$  ToF SIMS, and compared to  $\text{Cs}^+$  ion ToF SIMS,<sup>12</sup>  $\text{Ne}$ -ion ToF SIMS can offer higher lateral resolutions and smaller spot sizes which are important for correlative high resolution imaging. The Ne-SIMS maps in Figure 4 are of the same region of as the  $\text{He}^+$ -iSE and  $\text{Ne}^+$ -iSE images in Figure 4g,h. The SIMS maps clearly show that the CEI layer regions are rich in  $\text{Co}^+$ ,  $\text{PO}_2^-$ ,  $\text{Li}^+$ , and  $\text{O}^-$  ions compared to the binder- and C65-rich regions.  $\text{F}^-$  is more concentrated in the binder-rich regions compared to the CEI layer, but it is still present in the CEI layer.  $\text{C}^-$  appears

marginally more concentrated on the CEI layer regions than in the binder- and C65-rich regions.

$\text{Li}^+$  and  $\text{C}^-$  on the surface of the cathode could be ascribed to  $\text{R-OCO}_2\text{Li}$ ,  $\text{Li}_2\text{CO}_3$ , or organic components resulting from the degradation of the electrolyte solvent.<sup>16</sup>  $\text{Li}_2\text{CO}_3$  was found on the surface of  $\text{LiCoPO}_4$  after prolonged self-discharge,<sup>23</sup> while  $\text{R-OCO}_2\text{Li}$  is a typical degradation product of high voltage degradation of  $\text{LiPF}_6$  in EC and DMC electrolytes.<sup>12</sup>

Comparing the Ne-SIMS maps to the spectra in Figure 3 allows the origin of the fragments to be identified and provides a fingerprint of the structure and degree of system degradation.  $\text{PO}_2^-$  and  $\text{PO}_3^-$  ions originated from the  $\text{PO}_4$  tetrahedra in

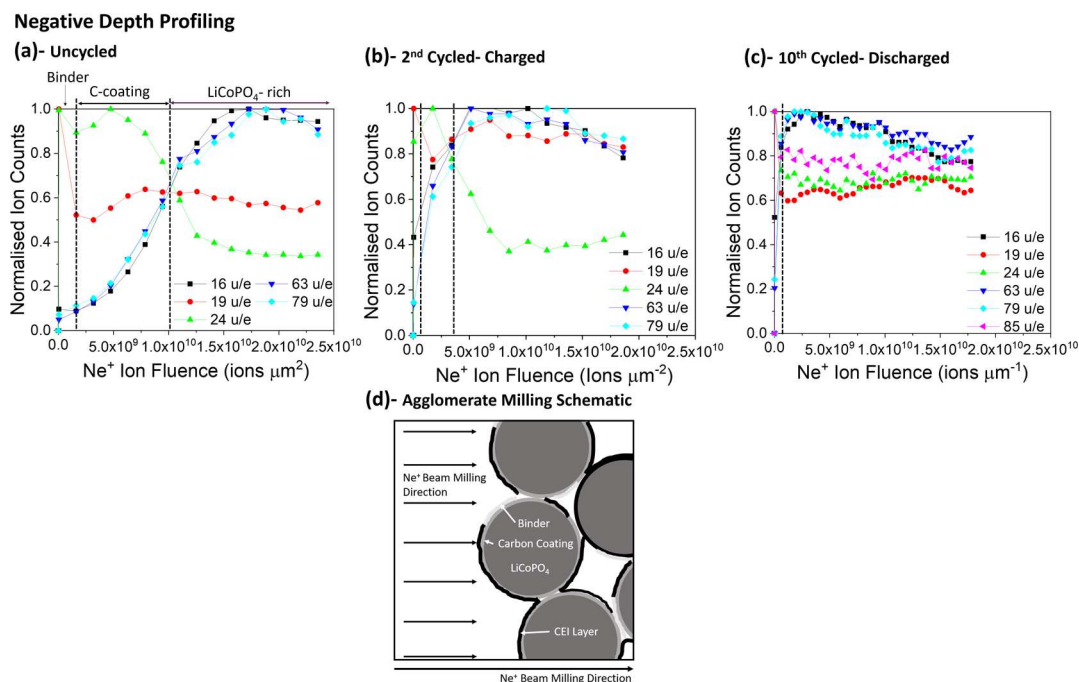


**Figure 6.** Negative Ne-SIMS depth profiles of the surface chemistry of C-LiCoPO<sub>4</sub> agglomerates. The ion fragment intensities have been normalized to the highest intensity of each ion fragment in the depth profile. Ion fluence was calculated as the product of beam current and milling time divided by the charge on a Ne<sup>+</sup> ion. The measurements have been performed on an uncycled electrode (a), on a two times cycled, charged electrode (b), and on a 10 times cycled, discharged electrode (c). Positive and negative SIMS were not performed at the same sample location. (d) Schematic of Ne<sup>+</sup>-SIMS depth profiling of a C-LiCoPO<sub>4</sub> agglomerate. The bottom arrow indicates the overall milling direction resulting from multiple Ne<sup>+</sup> beam rasters across the agglomerate surface. The ion milled area is larger than a single C-LiCoPO<sub>4</sub> primary particle. During a SIMS depth profile, the Ne-ion beam sputters down through the primary particle surfaces.

LiCoPO<sub>4</sub> in the uncycled electrode. However, in the cycled electrode, PO<sub>2</sub><sup>-</sup>, PO<sub>3</sub><sup>-</sup>, POF<sub>2</sub><sup>-</sup>, H<sub>2</sub>OF<sup>-</sup>, OF<sup>-</sup>, and LiF<sub>2</sub><sup>-</sup> are components of the CEI layer. These findings are consistent with the formation of surface PO<sub>2</sub>F<sub>y</sub> oxyfluorophosphates found,<sup>11</sup> and<sup>8</sup> oxyfluorophosphates result from nucleophilic attack of F<sup>-</sup> anions from the degraded electrolyte on the P atoms of LiCoPO<sub>4</sub>, resulting in the breaking of P–O bonds and formation of oxyfluorophosphates and LiPO<sub>2</sub>F<sub>2</sub>.<sup>8</sup>

C<sup>-</sup> is present in the binder and on the carbon coating of C-LiCoPO<sub>4</sub>, while O<sup>-</sup> originates from LiCoPO<sub>4</sub> and F<sup>-</sup> originates from the polyvinylidene fluoride (C<sub>2</sub>H<sub>2</sub>F<sub>2</sub>)<sub>n</sub> binder in the uncycled electrode. Li<sup>+</sup> and Co<sup>+</sup> are present in both the cycled and uncycled SIMS spectra (Figure 3b) and originate from LiCoPO<sub>4</sub> in the uncycled electrode. The origin of Li<sup>+</sup> and Co<sup>+</sup> in the cycled electrode could be from LiCoPO<sub>4</sub> or CEI components.

59 u/e has been identified as Co<sup>+</sup> on the positive SIMS spectra (Figure 3b), originating from LiCoPO<sub>4</sub> in the uncycled electrode. The peak is broad because of the broad energy distribution of ions sputtered from the bulk material. It should be noted that a previous study of high voltage CEI layers has attributed 59 u/e in cycled electrodes to <sup>7</sup>Li<sub>3</sub><sup>19</sup>F<sub>2</sub><sup>+</sup>.<sup>25</sup> It is possible that the 59 u/e peak from the cycled electrode contains both Co<sup>+</sup> and <sup>7</sup>Li<sub>3</sub><sup>19</sup>F<sub>2</sub><sup>+</sup> and that the broad peak could also be attributed to Li-6 and Li-7 isotopes of <sup>7</sup>Li<sub>3</sub><sup>19</sup>F<sub>2</sub><sup>+</sup>. It is possible that <sup>7</sup>Li<sub>3</sub><sup>19</sup>F<sub>2</sub><sup>+</sup> contributes to some of the intensity of the 59 u/e peak. However, there are no significant peaks in Figure 3b at 52 u/e for Li<sub>2</sub>F<sub>2</sub><sup>+</sup>, 45 u/e for LiF<sub>2</sub><sup>+</sup>, 40 u/e for Li<sub>3</sub>F<sub>2</sub><sup>+</sup> and 33 u/e for Li<sub>2</sub>F<sup>+</sup>. Therefore, it is unlikely that the majority of the contribution to the 59 u/e peak originates from <sup>7</sup>Li<sub>3</sub><sup>19</sup>F<sub>2</sub><sup>+</sup>. Ne-ion SIMS is also more likely to produce smaller ion fragments than Bi or Cs SIMS. A scan with a greater mass

resolution ( $M/\Delta M \sim 1000$ ) would help differentiate the 58.93 u/e fragment contribution from Co<sup>+</sup>, from the potential 58.82 u/e Li<sub>3</sub>F<sub>2</sub><sup>+</sup> fragment from the CEI.

**3.4. Cycling Behavior of the CEI Layer.** Gas field ion microscopy offers a new route to imaging of electrode interfaces in battery electrodes, including the CEI, and potential SEI layers in anodes, both by high spatial resolution helium ion imaging and neon ion ToF-SIMS analysis of the surface chemistry. Macro-scale imaging of the electrode enabled comparison between the underlying electrode microstructure and CEI growth.

CEI-sensitive He<sup>+</sup>-ion iSE images of the C-LiCoPO<sub>4</sub> electrode surfaces were taken under comparable imaging conditions at different cycle numbers to assess how the CEI layer microstructure varies with the cycle life (Figure 5). After being charged to 5.1 V versus Li/Li<sup>+</sup> on the 2nd, 5th, and 10th cycles, the CEI layer is clearly present (Figure 5a–c) visible as very low (black) iSE yield regions (Figure 5g), indicating that the layer forms at high voltages. Previous studies have reported that CEI layers form on LiCoPO<sub>4</sub> at potentials greater than 4.8 V versus Li/Li<sup>+</sup> using postmortem TEM and XPS.<sup>10,11</sup>

Comparing the charged and discharged electrode microstructures, there are no regions of very dark (black) contrast on the surface of the discharged electrode after the second cycle (Figure 5d,g), indicating that the CEI layer is either not present or very thin. After the 5th cycle, the CEI layer is visible in the discharged state (Figure 5e); however, regions of variable contrast (Figure 5g) indicate that they are of variable thicknesses. On the 10th cycle, in the discharge state, there is less contrast variability of the CEI layer regions than the 5th cycle, consistent with a thickening CEI layer and correlating

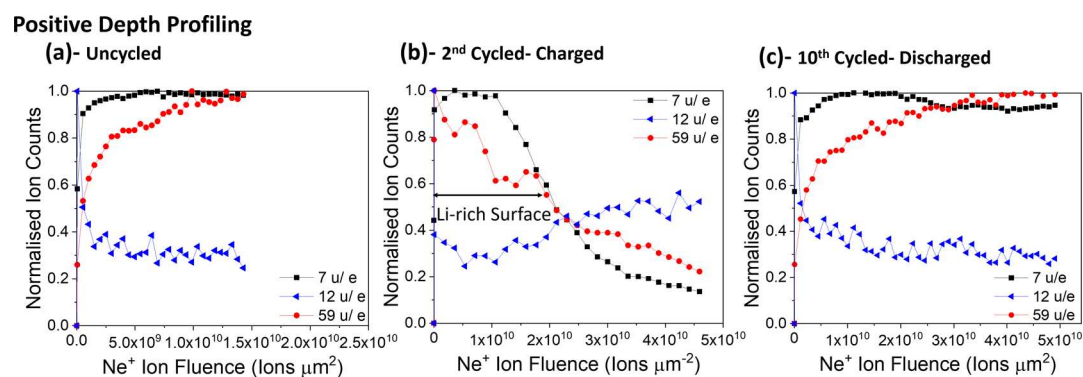


**Figure 7.** Ne-SIMS positive depth profiles of surface chemistry of C-LiCoPO<sub>4</sub> agglomerates. The ion fragment intensities have been normalized to the highest intensity of each ion fragment in the depth profile. Ion fluence was calculated as the product of beam current and milling time divided by the charge on a Ne<sup>+</sup> ion. The measurements have been performed on an uncycled electrode (a), on a two times cycled, charged electrode (b), and on a 10 times cycled, discharged electrode (c). Positive and negative SIMS were not performed at the same sample location.

with the measured increase in cell resistance and loss of cell capacity (Figure 1).

He-iSE imaging clearly shows that the CEI surface layer grows after charging to 5.1 V versus Li/Li<sup>+</sup> but dissolves after discharge to 2.5 V versus Li/Li<sup>+</sup>. After 2 cycles, the dissolution of the CEI is almost complete (Figure 5d), but the dissolution is only partial after the 5th and 10th cycles (Figure 5e,f). A CEI layer which undergoes dissolution would expose C-LiCoPO<sub>4</sub> (which has not previously touched electrolyte) to the electrolyte, potentially increasing degradation.

A porous and unstable CEI layer was reported by Manzi and Brutti;<sup>11</sup> however, this is the first time the LiCoPO<sub>4</sub> CEI layer has been imaged using He-ion microscopy, a technique enabling CEI thickness contrast, and chemically characterized at a high resolution using ToF SIMS to identify inhomogeneity across the whole electrode. Inhomogeneous formation of CEI layers has been proposed for other cathode materials using techniques such as NMR and EIS,<sup>26</sup> but He-ion microscopy allows direct imaging of the inhomogeneous CEI layer and its morphology with respect to the underlying electrode microstructure.

Formation of CEI is expected at high potentials as this is where electrolyte breakdown occurs. The dissolution of the CEI layer observed on discharge is likely the dissolution of soluble LiPO<sub>2</sub>F<sub>2</sub> discussed in refs.<sup>8,10</sup> Dissolution of the CEI layer will result in fresh LiCoPO<sub>4</sub> being exposed to further breakdown from parasitic reactions, and consumption of active LiCoPO<sub>4</sub> with the electrolyte leads to capacity drop (as observed in Figure 1).

An important result of the high spatial resolution He-ion imaging of the CEI layers is the determination that the CEI dissolution is not consistent across the electrode, resulting in variations in the thickness of the CEI layer (Figure 5). Close examination of the discharged electrode microstructures indicates that the regions showing incomplete CEI layer dissolution after discharge are predominantly on larger LiCoPO<sub>4</sub> agglomerates (Figure 5). This has not been previously reported likely because of the difficulty observing CEI layers clearly at the field of view which can image the electrode microstructure. A possible reason for locally accelerated CEI growth may be faster action by F<sup>-</sup> anions in the local presence of more LiCoPO<sub>4</sub>. It has been previously observed that binder materials can act as an HF scavenger,<sup>27</sup> which could help prevent further attack, although the PVDF used here is inefficient at absorbing HF.

### 3.5. Ne-SIMS Chemical Depth Profiling of Electrodes.

To evaluate the chemical evolution of the cycled electrodes in more detail, Ne-SIMS chemical depth profiling was performed on cycled C-LiCoPO<sub>4</sub> primary particle agglomerates with a surface CEI layer present (detected *in situ* using dark contrast regions on He<sup>+</sup> iSE images, e.g. Figure 2). A schematic of the microstructure of the cycled C-LiCoPO<sub>4</sub> agglomerate electrode surface is shown in Figure 6g. Cycled electrode agglomerates consist of 300 nm carbon-coated LiCoPO<sub>4</sub> primary particles, infiltrated binders, and CEI layers. Figure 6g illustrates the fact that the Ne-SIMS depth profiles will contain sputtered ion fragments originating from the binder, CEI layer, primary particle carbon coating, and LiCoPO<sub>4</sub> particles throughout the measured milling time. The lateral width of the scanned areas (~1 μm<sup>2</sup>) was larger than one LiCoPO<sub>4</sub> primary particle; hence, more than one was depth was profiled. Depth profiling was performed on up to three separate regions of the sample for each condition. The presence of ion fragments identified in Figure 3 was consistent across all areas. The SIMS depth-profiling results in Figures 6 and 7 are of representative regions of LiCoPO<sub>4</sub> agglomerates.

The Ne-SIMS depth profiles are plotted as measured ion yield normalized by the maximum count for a given fragment, against the Ne<sup>+</sup> ion fluence (product of the beam current and milling time, divided by the milling area). The measured areas were 1 μm × 1 μm for all the regions of interest (ROIs), except for the 10th cycle discharged electrode negative ROI (1.5 × 1.5 μm) and the uncycled positive ROI (0.5 × 0.5 μm). Plotting against Ne<sup>+</sup> ion fluence normalized the measurement regions, accounting for the ROI area discrepancy. The complexity of the cathode surface and lack of depth profile standards made calculating the absolute sample concentration and measuring the sputtering depth not feasible.

The ions analyzed in the negative Ne-SIMS depth profiles from C-LiCoPO<sub>4</sub> electrodes are 16 u/e (<sup>16</sup>O<sup>-</sup>), 19 u/e (<sup>19</sup>F<sup>-</sup>), 24 u/e (<sup>12</sup>C<sub>2</sub><sup>-</sup>), 63 u/e (<sup>31</sup>P<sup>16</sup>O<sub>2</sub><sup>-</sup>), 79 u/e (<sup>31</sup>P<sup>16</sup>O<sub>3</sub><sup>-</sup>), and 85 u/e (<sup>31</sup>P<sup>16</sup>O<sup>19</sup>F<sub>2</sub><sup>-</sup>) (Figure 6a–c). Table 1 identifies the electrode constituents from which these fragments originate. <sup>16</sup>O<sup>-</sup> and <sup>19</sup>F<sup>-</sup> were chosen as these are the most intense peaks in the Ne-SIMS spectra (Figure 3a). <sup>12</sup>C<sub>2</sub><sup>-</sup> was chosen to represent carbon as the O<sup>-</sup> peak overlapped with the C<sup>-</sup> peak when the O<sup>-</sup> peak intensity increased during depth profiling. PO<sub>2</sub><sup>-</sup>, PO<sub>3</sub><sup>-</sup>, and POF<sub>2</sub><sup>-</sup> were analyzed as the ion yield increased significantly on the cycled electrode compared to the uncycled electrode (Figure 3a).

**Table 1.** Ion Fragment  $m/z$  Ratios in the Depth Profiles in Figure 6, the Associated Ions, and the Origin of the Fragments Measured in the Depth Profiles

negative SIMS depth profile ions		
$m/z$	ion	origin
16 u/e	O <sup>-</sup>	LiCoPO <sub>4</sub>
19 u/e	F <sup>-</sup>	binder/CEI
24 u/e	C <sub>2</sub> <sup>-</sup>	C6S/binder/CEI/C-coating
63 u/e	PO <sub>2</sub> <sup>-</sup>	LiCoPO <sub>4</sub> /CEI
79 u/e	PO <sub>3</sub> <sup>-</sup>	LiCoPO <sub>4</sub> /CEI
85 u/e	POF <sub>2</sub> <sup>-</sup>	CEI

The transitions between the highest yield of F<sup>-</sup>, C<sub>2</sub><sup>-</sup>, and O<sup>-</sup>, PO<sub>2</sub><sup>-</sup>, and PO<sub>3</sub><sup>-</sup> ion fragments on the uncycled negative Ne-SIMS depth profile, Figure 6a, clearly indicate the existence of the binder-rich, carbon coating-rich, and LiCoPO<sub>4</sub>-rich layers sequentially. Sputtering into the uncycled electrode Figure 6a, initially, F<sup>-</sup> is high, indicating a thin layer of the surface binder. The C<sub>2</sub><sup>-</sup> yield remains high as the F<sup>-</sup> yield drops indicating milling of the carbon coating layer on the LiCoPO<sub>4</sub> particles. O<sup>-</sup>, PO<sub>2</sub><sup>-</sup>, and PO<sub>3</sub><sup>-</sup> have the highest yield toward the end of the depth profile, indicating bulk LiCoPO<sub>4</sub>. The yields of ion fragments of the binder and carbon layer (F<sup>-</sup>, and C<sub>2</sub><sup>-</sup> respectively) do not drop to zero because of these components being present within the porous agglomerate (see Figure 6g).

On the cycled electrodes, the CEI layer is present on the C-LiCoPO<sub>4</sub> agglomerates (as identified in the He<sup>+</sup> iSE images, Figure 5a–c). The negative Ne-SIMS depth profiles of the cycled electrodes (Figure 6b,c) identify the presence of POF<sub>2</sub><sup>-</sup> on the surface, which was not present in the uncycled electrode (Figure 6a). The yield of F<sup>-</sup> and POF<sub>2</sub><sup>-</sup> follows similar patterns, with both fragments exhibiting relatively constant concentrations throughout the milling. The presence of POF<sub>2</sub><sup>-</sup> at the surface is consistent with the presence of a CEI layer.

Sputtering into the 2nd cycle charged electrodes, the Ne-SIMS depth profiles (Figure 6b) show that the highest yields of F<sup>-</sup>, C<sub>2</sub><sup>-</sup>, and O<sup>-</sup>, PO<sub>2</sub><sup>-</sup>, and PO<sub>3</sub><sup>-</sup> occur in a similar sequence to the uncycled electrode. However, the yields of O<sup>-</sup>, PO<sub>2</sub><sup>-</sup>, and PO<sub>3</sub><sup>-</sup> increase more rapidly during depth profiling on the second cycle-charged sample (Figure 6b) compared to the uncycled electrode (Figure 6a). The yields of O<sup>-</sup>, PO<sub>2</sub><sup>-</sup>, and PO<sub>3</sub><sup>-</sup> increase with depth to their maximum as the yield of C<sub>2</sub><sup>-</sup> decreases to the minimum yield (Figure 6a), whereas the maximum yield in the uncycled electrode of O<sup>-</sup>, PO<sub>2</sub><sup>-</sup>, and PO<sub>3</sub><sup>-</sup> occurs after the C<sub>2</sub><sup>-</sup> yield drops to the minimum (Figure 6a). These differences imply changes (potentially chemical intermixing) to the carbon coating layer during cycling.

Comparing the 2nd cycle charged electrode (Figure 6b), with the 10th cycle discharged electrode (Figure 6c), the transition to the highest O<sup>-</sup>, PO<sub>2</sub><sup>-</sup>, PO<sub>3</sub><sup>-</sup> and the lowest C<sub>2</sub><sup>-</sup> yield occurs after less Ne<sup>+</sup> ion fluence in the 10th cycle discharged electrode. This indicates further chemical changes to the original carbon coating and surface interfaces are progressive with increased cycling.

The Ne-SIMS depth profiling of the CEI layer on LiCoPO<sub>4</sub> shows that the CEI is composed of LiPF<sub>6</sub> decomposition products (oxyfluorophosphates), consistent with XPS results.<sup>8,11</sup> The results are similar to ToF SIMS analysis of high voltage spinel LiMn<sub>1.5</sub>Ni<sub>0.5</sub>O<sub>4</sub> by Manthiram et al. which forms an unstable CEI resulting from operating outside the electrolyte stability potential window.<sup>28</sup> Other high voltage

cathode materials, such as nickel-rich layered lithium nickel manganese cobalt oxides, show significant decomposed organic species, and the layer itself is typically more stable than those formed from decomposed LiPF<sub>6</sub> species.<sup>28</sup> Overall, the CEI analysis presented here by HIM-SIMS confirms that CEI layers formed from decomposition of LiPF<sub>6</sub> electrolyte components are unstable, resulting in partial dissolution of the CEI during cycling. CEI stability could be improved by stabilizing the decomposition reaction of the electrolyte.

The ions analyzed in the positive Ne-SIMS depth profiles from C-LiCoPO<sub>4</sub> electrodes are 7 u/e (<sup>7</sup>Li<sup>+</sup>), 12 u/e (<sup>12</sup>C<sup>+</sup>), and 59 u/e (<sup>59</sup>Co<sup>+</sup>) (Figure 7a–c and described in Table 2).

**Table 2.** Ion Fragment  $m/z$  Ratios in the Depth Profiles in Figure 7 and the Associated Ions

positive SIMS depth profile ions	
$m/z$	ion
7 u/e	Li <sup>+</sup>
12 u/e	C <sup>+</sup>
59 u/e	Co <sup>+</sup> /Li <sub>3</sub> F <sub>2</sub> <sup>+</sup>

Li<sup>+</sup> was analyzed to evaluate if Li was being fully cycled in the electrode, and C<sup>+</sup> was measured as a representative of the carbon-coating layer. The ionization efficiency of C in positive SIMS is less than in negative SIMS, so the C trends in the positive SIMS depth profiles (Figure 7a–c) do not match the negative depth profiles (Figure 6a–c). As discussed previously in Section 3.3, 59 u/e ion fragments could originate from either <sup>59</sup>Co<sup>+</sup> or <sup>7</sup>Li<sub>3</sub><sup>19</sup>F<sub>2</sub><sup>+</sup> or contributions from both, although the contribution from Co<sup>+</sup> is likely stronger.

Lithium is expected near the surface of uncycled electrodes and any discharged electrodes because the discharged state of LiCoPO<sub>4</sub> is LiCoPO<sub>4</sub>.<sup>29</sup> Ne-SIMS depth profiling of the ions sputtered from the uncycled C-LiCoPO<sub>4</sub> agglomerate shows that Li<sup>+</sup> yield increases rapidly to reach a maximum signal after a Ne<sup>+</sup> ion fluence of 6.92 × 10<sup>9</sup> ions μm<sup>-2</sup> (Figure 7a). The 10th cycle discharged electrode, known to have a surface CEI layer, also exhibits an increase in Li<sup>+</sup> yield below the surface (Figure 7c), although the maximum Li<sup>+</sup> yield occurs after milling with a greater Ne<sup>+</sup> ion fluence of 1.12 × 10<sup>10</sup> ions μm<sup>-2</sup>. The delay in maximum Li<sup>+</sup> yield at the 10th cycle discharged electrode is consistent with the thickening CEI on cycling, as imaged by HIM (Figure 5).

It should be noted that sputtered Li<sup>+</sup> ions are detected at all sputtered depths, corresponding to both the carbon-coating in the uncycled electrode, and the CEI layer in the 10th cycle discharged electrode (Figure 7a–c).

Lithium is not expected to be present in the charged electrodes, as the charged state of LiCoPO<sub>4</sub> is CoPO<sub>4</sub>.<sup>29</sup> However, sputtering into the 2nd cycle charged electrode, a steady increase in Li<sup>+</sup> yield is observed with depth, reaching a maximum after milling with 3.59 × 10<sup>9</sup> ions μm<sup>-2</sup> (Figure 6e). The Li<sup>+</sup> yield then steadily decreases with depth away from the surface, indicating a Li-rich surface region.

Accumulation of Li would result in capacity loss, as observed in the electrochemical testing of the same electrodes (Figure 1). The surface lithium lies both in the CEI layer and at the surface of the charged electrode agglomerates. The charged state of LiCoPO<sub>4</sub> is CoPO<sub>4</sub>, so theoretically, there should not have been Li present in the agglomerates. Manzi et al. have previously found evidence for spontaneous reincorporation of Li into the *Pnma* CoPO<sub>4</sub> lattice as a result of the instability of

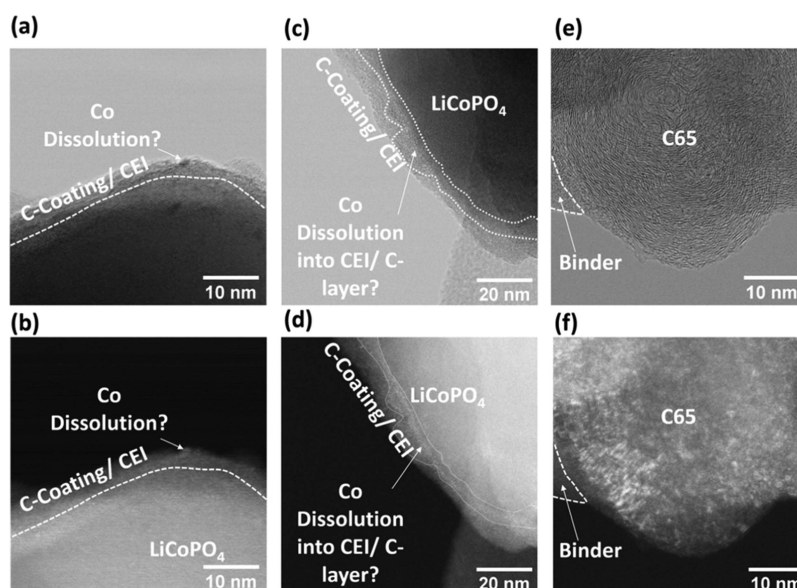


**Figure 8.** BF (a, c, e) and HAADF (b, d, f) images of 10th cycle discharged, (a–d) LiCoPO<sub>4</sub> particles, and (e,f) C65, conductive additive particle.

an octahedrally coordinated Co<sup>3+</sup> ion in a high spin-state in the lattice.<sup>11</sup>

Considering the positive Ne-SIMS depth profiles of the 59 u/e ion fragments (Co<sup>+</sup> or Li<sub>3</sub>F<sub>2</sub><sup>+</sup>), the 59 u/e yield steadily increases with Ne<sup>+</sup> ion fluence/depth in both the uncycled electrode (Figure 7a) and the 10th cycle discharged electrode (Figure 7c). However, the 59 u/e gradual increase occurs after milling with increased ion fluence in the 10th cycle discharged electrode. This trend is consistent with 59 u/e being sputtered with Co<sup>+</sup> ions, as the ion beam mills into LiCoPO<sub>4</sub>-rich particles with increasing depth (as shown on Figure 6d).

The Ne-SIMS depth profile from the 2nd cycle charged electrodes both has the highest yield of 59 u/e at the outer surface of the electrode (Figure 7b) and a decreasing yield of 59 u/e thereafter as the Ne-beam sputters deeper into the electrode surface. The charged sample results are surprising if the 59 u/e signal originates solely from Co<sup>+</sup> ions because the Co<sup>+</sup> yield should increase to a maximum when ion milling reaches the LiCoPO<sub>4</sub>-rich and CoPO<sub>4</sub>-rich regions in the discharged and charged samples, respectively. The high yield of 59 u/e at the outer surface of the charged electrodes could arise from the additional contribution of Li<sub>3</sub>F<sub>2</sub><sup>+</sup> ions arising from the growing CEI layer, Co dissolution into the carbon layer and CEI, or a mixture of both.

**3.6. STEM Examination of the C-LiCoPO<sub>4</sub> Primary Particles.** To examine at higher resolution, the growth of persistent CEI layers on the cycled C-LiCoPO<sub>4</sub> agglomerates and the interplay of the CEI with the original carbon coating, the 10th cycle discharged LiCoPO<sub>4</sub> electrodes were examined by HAADF and bright-field (BF) STEM. Figure 8 shows representative images of LiCoPO<sub>4</sub> primary particles (Figure 8a–d) and the conductive additive (C65) and binder (Figure 8e,f). LiCoPO<sub>4</sub> appears bright in the HAADF images (Figure 8a,c) and dark in the BF images (Figure 8b,d).

STEM images of the 10th cycle discharged LiCoPO<sub>4</sub> particles (Figure 8a–d) show a coating on the surface of the LiCoPO<sub>4</sub>. The coating was of variable thickness, measuring ~6 nm in Figure 8a,b, while in Figure 8c,d, the coating is 8–20 nm thick. The post-cycling 6–20 nm surface layer is thicker than the original 2–8 nm carbon coating thickness on the surface of

the LiCoPO<sub>4</sub> particles, consistent with being a mixture of the CEI layer and carbon coating identified by SIMS depth profiles in Figures 6 and 7.

Close examination of the coating microstructure revealed inhomogeneous HAADF contrast, in particular, a bright band of contrast being frequently visible at the interface between the coating and LiCoPO<sub>4</sub> (e.g. Figure 8d) and discrete bright regions <10 nm in the C-coating in Figure 8b. The BF images show dark regions (significant electron scattering) corresponding to the bright regions in the HAADF images (Figure 8a,b). These contrast changes are consistent with local variations in composition, composed of a higher concentration of the heavy element (Co dissolved from the adjacent LiCoPO<sub>4</sub>) consistent with the surface Co detected in the Ne-SIMS depth profiles (Figure 7a–c). Co dissolution in other high voltage cathode materials has been previously identified by ToF-SIMS by finding CoF<sub>3</sub><sup>+</sup> fragments because of the reaction of Co with the electrolyte.<sup>12</sup> CoF<sub>3</sub><sup>+</sup> was not detected in this study (Figure 3b). In addition, the local variations in coating thickness may also contribute to increased local scattering.

Here, no evidence of a detectable CEI layer forming on the conductive additive region has been observed through HIM, SEM, or STEM (Figures 2, and 8). STEM BF imaging of the conductive additive (C65 particles) after 10 cycles, showed their typical graphite onion structure (Figure 8e). A corresponding HAADF image (Figure 8f) shows bright contrast regions embedded within the concentric graphite-like structure, which result from heavy metal impurities in the carbon black. STEM imaging showed no evidence of a film forming on the C65 particles as a result of cycling the electrode, consistent with the distinct contrast of the CEI layer found on C–LiCoPO<sub>4</sub> agglomerates imaged by HIM (Figure 2b).

Overall, the analysis of the high-voltage electrodes as a function of electrochemical history demonstrates a requirement for high-resolution imaging of CEI layers and the local microstructure, coupled with chemical correlation. The techniques of helium ion imaging coupled with Ne-ion ToF-SIMS are able to evaluate electrode microstructural evolution, shedding light on degradation mechanisms and hence aiding

optimization of electrode design. CEI distribution mapping is possible by high-resolution ToF SIMS mapping, as demonstrated by Manthiram et al.,<sup>12,28</sup> however, the addition of correlative He-ion imaging used here also allows evaluation of CEI thickness and surface topography and hence correlation of the CEI morphology with the CEI chemistry.

#### 4. CONCLUSIONS

This study has used HIM for the first time to achieve high-resolution He-iSE images of CEI layers on LiCoPO<sub>4</sub>. He-iSE imaging enabled visualization of the CEI at a field of view which allows for comparison of the CEI distribution with the underlying electrode microstructure and imaging of the variation in CEI layer thickness. *In situ* Ne-ion ToF-SIMS analysis generates site-specific chemical characterization of the electrode surfaces, allowing correlation of the observed morphological changes with chemical changes of the CEI layer.

The helium ion imaging and *in situ* Ne-ion ToF-SIMS demonstrate that degradation of C-LiCoPO<sub>4</sub> is partly caused by the formation of an unstable CEI layer on C-LiCoPO<sub>4</sub> agglomerates. The CEI layer is rich in oxyfluorophosphates, and there is evidence of a Li-rich surface and possible Co dissolution on the surface of the electrode. Helium ion imaging of electrodes at different points in their cycle life has confirmed that the CEI layer is unstable, forming on charge and partially dissolving on discharge and leaving LiCoPO<sub>4</sub> vulnerable to further degradation from the electrolyte. However, the high spatial resolution achievable using He-iSE imaging has shown that the CEI is spatially inhomogeneous, with variable thickness on larger agglomerates which show evidence of localized CEI thinning.

Overall, the results highlight the benefit of new techniques such as HIM-SIMS, which are capable of both high-resolution imaging and chemical characterization of electrode surface degradation phenomena, to correlate the underlying electrode microstructure with CEI formation processes. HIM-SIMS identification of CEI inhomogeneity will benefit growing research on control of cathode microstructures and use of novel electrode components which can aid cycle life improvements. For LiCoPO<sub>4</sub>, use of the HIM-SIMS technique could be used to understand CEI formation and inhomogeneity in full-cell configuration, with electrode structures and components optimized to reduce CEI inhomogeneity and using electrolyte additives to stabilize the CEI layer.

#### ■ ASSOCIATED CONTENT

##### SI Supporting Information

The Supporting Information is available free of charge at <https://pubs.acs.org/doi/10.1021/acsaem.0c01333>.

Galvanostatic cycling, and differential capacity curves for the first cycle, galvanostatic discharge curves showing the effect of calendaring; X-ray diffraction patterns uncycled electrodes and electrodes charged to 5.1 V versus Li/Li<sup>+</sup> showing the expected phases; TEM imaging and associated selected area electron diffraction of an uncycled particle; and explanation of the effect of air exposure on the results including SEM imaging of 1 week air exposed and 1 min air exposed samples (PDF)

#### ■ AUTHOR INFORMATION

##### Corresponding Author

Laura Wheatcroft – Department of Materials Science and Engineering, University of Sheffield, Sheffield S1 3JD, U.K.; [orcid.org/0000-0003-2306-9791](https://orcid.org/0000-0003-2306-9791); Email: [l.j.wheatcroft@sheffield.ac.uk](mailto:l.j.wheatcroft@sheffield.ac.uk)

##### Authors

Nico Klingner – Helmholtz Zentrum Dresden-Rossendorf, Dresden 01328, Germany; [orcid.org/0000-0001-9539-5874](https://orcid.org/0000-0001-9539-5874)

René Heller – Helmholtz Zentrum Dresden-Rossendorf, Dresden 01328, Germany

Gregor Hlawacek – Helmholtz Zentrum Dresden-Rossendorf, Dresden 01328, Germany; [orcid.org/0000-0001-7192-716X](https://orcid.org/0000-0001-7192-716X)

Doğan Özkaya – Johnson Matthey Technology Centre, Reading RG4 9NH, U.K.

James Cookson – Johnson Matthey Technology Centre, Reading RG4 9NH, U.K.

Beverley J. Inkson – Department of Materials Science and Engineering, University of Sheffield, Sheffield S1 3JD, U.K.; [orcid.org/0000-0002-2631-9090](https://orcid.org/0000-0002-2631-9090)

Complete contact information is available at: <https://pubs.acs.org/10.1021/acsaem.0c01333>

##### Author Contributions

The manuscript was written through contributions of all authors. All authors have given approval to the final version of the manuscript.

##### Notes

The authors declare no competing financial interest.

#### ■ ACKNOWLEDGMENTS

Part of this research was carried out at the Ion Beam Center (IBC) at the Helmholtz-Zentrum Dresden-Rossendorf e. V., a member of the Helmholtz Association. The authors acknowledge the Leverhulme Trust: PicoFIB Network, under grant IN-2016-027, for support to carry out Gas-Ion Microscopy and Johnson Matthey for providing LiCoPO<sub>4</sub>. The EPSRC under grant EP/L016818/1, The Energy Storage CDT at the University of Sheffield, and Johnson Matthey are thanked for a PhD studentship (L.W.).

#### ■ ABBREVIATIONS

HIM, helium ion microscopy  
ToF-SIMS, time of flight secondary ion mass spectrometry  
SEM, scanning electron microscopy  
S/TEM, scanning/transmission electron microscopy  
HAADF, high angle annular dark field  
BF, bright field  
eSE, electron induced secondary electrons  
iSE, ion induced secondary electrons  
He-iSE, Helium-ion induced secondary electrons  
Ne-iSE, Neon-ion induced secondary electrons  
BSE, backscattered electrons  
ETD, Everhart-Thornley detector  
ILD, In-lens detector  
CEI, cathode electrolyte interphase  
SEI, solid electrolyte interphase  
LCP, LiCoPO<sub>4</sub>  
C-LiCoPO<sub>4</sub>, carbon coated LiCoPO<sub>4</sub>

PVDF, polyvinylidene fluoride binder  
C65, conductive additive used in electrode

## REFERENCES

- (1) Bruce, P. G.; Freunberger, S. A.; Hardwick, L. J.; Tarascon, J.-M. Li-O<sub>2</sub> and Li-S batteries with high energy storage. *Nat. Mater.* **2012**, *11*, 19–29.
- (2) Gür, T. M. Review of electrical energy storage technologies, materials and systems: Challenges and prospects for large-scale grid storage. *Energy Environ. Sci.* **2018**, *11*, 2696–2767.
- (3) Hu, M.; Pang, X.; Zhou, Z. Review Recent progress in high-voltage lithium ion batteries. *J. Power Sources* **2013**, *237*, 229–242.
- (4) Amine, K.; Yasuda, H.; Yamachi, M. Olivine LiCoPO<sub>4</sub> as 4.8 V electrode material for lithium batteries. *Electrochem. Solid-State Lett.* **2000**, *3*, 178–179.
- (5) Zhang, M.; Garcia-Araez, N.; Hector, A. L. Understanding and development of olivine LiCoPO<sub>4</sub> cathode materials for lithium-ion batteries. *J. Mater. Chem. A* **2018**, *6*, 14483–14517.
- (6) Truong, Q. D.; Devaraju, M. K.; Tomai, T.; Honma, I. Direct Observation of Antisite Defects in LiCoPO<sub>4</sub> Cathode Materials by Annular Dark- and Bright-Field Electron Microscopy. *ACS Appl. Mater. Interfaces* **2013**, *5*, 9926–9932.
- (7) Boulineau, A.; Gutel, T. “Revealing Electrochemically Induced Antisite Defects in LiCoPO<sub>4</sub>: Evolution upon Cycling. *Chem. Mater.* **2015**, *27*, 802–807.
- (8) Markevich, E.; Sharabi, R.; Gottlieb, H.; Borgel, V.; Fridman, K.; Salitra, G.; Aurbach, D.; Semrau, G.; Schmidt, M. A.; Schall, N.; Bruenig, C. Reasons for capacity fading of LiCoPO<sub>4</sub> cathodes in LiPF<sub>6</sub> containing electrolyte solutions. *Electrochem. Commun.* **2012**, *15*, 22–25.
- (9) Sharabi, R.; Markevich, E.; Borgel, V.; Salitra, G.; Gershinsky, G.; Aurbach, D.; Semrau, G.; Schmidt, M. A.; Schall, N.; Stinner, C. Raman study of structural stability of LiCoPO<sub>4</sub> cathodes in LiPF<sub>6</sub> containing electrolytes. *J. Power Sources* **2012**, *203*, 109–114.
- (10) Markevich, E.; Salitra, G.; Fridman, K.; Sharabi, R.; Gershinsky, G.; Garsuch, A.; Semrau, G.; Schmidt, M. A.; Aurbach, D. Fluoroethylene Carbonate as an Important Component in Electrolyte Solutions for High-Voltage Lithium Batteries: Role of Surface Chemistry on the Cathode. *Langmuir* **2014**, *30*, 7414–7424.
- (11) Manzi, J.; Brutti, S. Surface chemistry on LiCoPO<sub>4</sub> electrodes in lithium cells: SEI formation and self-discharge. *Electrochim. Acta* **2016**, *222*, 1839–1846.
- (12) Li, W.; Dolocan, A.; Oh, P.; Celio, H.; Park, S.; Cho, J.; Manthiram, A. Dynamic behaviour of interphases and its implication on high-energy-density cathode materials in lithium-ion batteries. *Nat. Commun.* **2017**, *8*, 14589.
- (13) Wang, Y.; Ming, H.; Qiu, J.; Yu, Z.; Li, M.; Zhang, S.; Yang, Y. Improving cycling performance of LiCoPO<sub>4</sub> cathode material by adding tris(trimethylsilyl) borate as electrolyte additive. *J. Electroanal. Chem.* **2017**, *802*, 8–14.
- (14) Zampardi, G.; La Mantia, F. Solid-Electrolyte Interphase at the Positive Electrodes in High Energy Li-ion Batteries: Current Understanding and Analytical Tools. *Batteries Supercaps* **2020**, *3*, 672.
- (15) Tan, S.; Livengood, R.; Shima, D.; Notte, J.; McVey, S. Gas field ion source and liquid metal ion source charged particle material interaction study for semiconductor nanomachining applications. *J. Vac. Sci. Technol., B* **2010**, *28*, C6F15–C6F21.
- (16) Wirtz, T.; De Castro, O.; Audinot, J.-N.; Philipp, P. Imaging and Analytics on the Helium Ion Microscope. *Annu. Rev. Anal. Chem.* **2019**, *12*, 523–543.
- (17) Scipioni, L.; Sanford, C. A.; Notte, J.; Thompson, B.; McVey, S. Understanding imaging modes in the helium ion microscope. *J. Vac. Sci. Technol., B: Microelectron. Nanometer Struct* **2009**, *27*, 3250–3255.
- (18) Hlawacek, G.; Götzhäuser, A. *Helium Ion Microscopy*; Springer, 2016.
- (19) Klingner, N.; Heller, R.; Hlawacek, G.; Facsko, S.; von Borany, J. Time-of-flight secondary ion mass spectrometry in the helium ion microscope. *Ultramicroscopy* **2019**, *198*, 10–17.
- (20) Klingner, N.; Heller, R.; Hlawacek, G.; Borany, J. v.; Notte, J.; Huang, J.; Facsko, S. Nanometer scale elemental analysis in the helium ion microscope using time of flight spectrometry. *Ultramicroscopy* **2016**, *162*, 91–97.
- (21) Sharabi, R.; Markevich, E.; Borgel, V.; Salitra, G.; Aurbach, D.; Semrau, G.; Schmidt, M. A.; Schall, N.; Stinner, C. Significantly improved cycling performance of LiCoPO<sub>4</sub> cathodes. *Electrochem. Commun.* **2011**, *13*, 800–802.
- (22) Devaraju, M.; Truong, Q.; Hyodo, H.; Tomai, T.; Honma, I. Supercritical Fluid Synthesis of LiCoPO<sub>4</sub> Nanoparticles and Their Application to Lithium Ion Battery. *Inorganics* **2014**, *2*, 233–247.
- (23) Manzi, J.; Vitucci, F. M.; Paolone, A.; Trequattrini, F.; Di Lecce, D.; Panero, S.; Brutti, S. Analysis of the self-discharge process in LiCoPO<sub>4</sub> electrodes: bulks. *Electrochim. Acta* **2015**, *179*, 604–610.
- (24) Goodenough, J. B.; Kim, Y. Challenges for Rechargeable Li Batteries †. *Chem. Mater.* **2010**, *22*, 587–603.
- (25) Vidal Laveda, J.; Low, J. E.; Pagani, F.; Stilp, E.; Dilger, S.; Baran, V.; Heere, M.; Battaglia, C. Stabilizing Capacity Retention in NMC811/Graphite Full Cells via TMSPi Electrolyte Additives. *ACS Appl. Energy Mater.* **2019**, *2*, 7036–7044.
- (26) Dupré, N.; Martin, J.-F.; Oliveri, J.; Soudan, P.; Guyomard, D.; Yamada, A.; Kanno, R. Aging of the LiNi<sub>1/2</sub>Mn<sub>1/2</sub>O<sub>2</sub> positive electrode interface in electrolyte. *J. Electrochem. Soc.* **2009**, *156*, C180.
- (27) Kim, E. J.; Yue, X.; Irvine, J. T. S.; Armstrong, A. R. Improved electrochemical performance of LiCoPO<sub>4</sub> using eco-friendly aqueous binders. *J. Power Sources* **2018**, *403*, 11–19.
- (28) Erickson, E. M.; Li, W.; Dolocan, A.; Manthiram, A. Insights into the Cathode-Electrolyte Interphases of High-Energy-Density Cathodes in Lithium-Ion Batteries. *ACS Appl. Mater. Interfaces* **2020**, *12*, 16451–16461.
- (29) Strohbridge, F. C.; Clément, R. J.; Leskes, M.; Middlemiss, D. S.; Borkiewicz, O. J.; Wiaderek, K. M.; Chapman, K. W.; Chupas, P. J.; Grey, C. P. Identifying the Structure of the Intermediate, Li<sub>2/3</sub>CoPO<sub>4</sub>, Formed during Electrochemical Cycling of LiCoPO<sub>4</sub>. *Chem. Mater.* **2014**, *26*, 6193–6205.